AIAA/AAS Astrodynamics Specialist Conference
13 - 16 August 2012, Minneapolis, Minnesota

AIAA 2012-4434

An Adaptive, Receding-Horizon Guidance Strategy for Solar Sail Trajectories

Geoffrey G. Wawrzyniak*
a.i. solutions, Inc., Lanham, Maryland 20706, USA

Kathleen C. Howell†
Purdue University, West Lafayette, Indiana 47907, USA

Without additional attitude and orbital control systems, such as thrusters, solar-sail trajectories are controlled by the orientation of the sailcraft. The sail attitude is employed to target the sailcraft to some future state along the reference trajectory. In a "turn-and-hold" strategy, the attitude profile consists of at least three orientations between an initial and future, target state along the trajectory. Because of orbit-knowledge, control, and turn-modeling errors, a look-ahead control strategy is generated, one in which only the first turn from the profile is performed, and then a new profile is constructed based on updated orbit knowledge. The initial hold intervals, along with the number of turns, used to generate an attitude profile is automatically adapted to improve convergence of the algorithm. This technique is generally successful when applied to reference trajectories generated in an Earth–Moon–Sun ephemeris regime.

I. Introduction

RECENT in-space demonstrations of solar sails include both interplanetary (JAXA's IKAROS)[1] and low-Earth orbiting (NASA's NanoSail-D2)[2] applications. Additionally, at least two solar sail technology demonstration missions are in development. The Planetary Society's LightSail-1™ has completed qualification testing and awaits a ride on a launch vehicle,[3] and NASA's Office of the Chief Technologist has selected a large (100 m by 100 m) solar sail for demonstration at the Sun–Earth sub-L_1 point.[4]

As solar sail technology advances, that is, the mass-to-area ratio of the sail decreases, the portfolio of mission applications expands.[5] One such application employs the sail to create a "hover" orbit, whereby the sailcraft is in continuous view of a station located at the lunar south pole.[6,7] The dynamical regime for this application, involving gravity effects from multiple bodies as well as a large contribution from solar radiation pressure, is only recently investigated and, in those investigations, by means of numerical techniques. The resulting trajectories are coupled to a continuous re-orientation strategy that enables the vehicle to fly along a non-Keplerian orbit offset from the center of the Moon.

These offset, non-Keplerian orbits are unstable. Solar radiation pressure is more than a perturbation; it is a control force, effectively "balancing" the gravitational attraction of multiple bodies while the sailcraft is in motion. Even with the highest-fidelity force modeling, any error or uncertainty in the model may cause the vehicle to diverge from its intended path. Therefore, it is beneficial to consider the hover orbits as reference trajectories in that they closely approximate a solution to the equations of motion. As a consequence, an additional control law is required to follow the desired path.

In existing work by Wawrzyniak and Howell,[8] a look-ahead, or receding-horizon, strategy based on regular, discrete turn events is proposed (as opposed to continuously re-orienting the vehicle is proposed). A fixed number of days between reorientation events and a fixed number of turns are used in generating

*Worked performed as a Ph.D. candidate at Purdue University in the School of Aeronautics and Astronautics; currently employed as Project Engineer, a.i. solutions, Inc., Mission Services Division, 10001 Derekwood Lane, Suite 215, Lanham, Maryland 20706, USA.

†Hsu Lo Professor of Aeronautical and Astronautical Engineering, Purdue University, School of Aeronautics and Astronautics, 701 Stadium Ave., West Lafayette, Indiana 47907, USA.

an attitude profile along an arc along the reference trajectory. The *arc* spans the portion of the trajectory from the present state to a target state. The turns delimit the subarcs within an arc. A multiple-shooting technique is exploited to determine the appropriate solar sail orientations along trajectory subarcs necessary to follow a reference path. However, only the first turn-and-hold subarc (the portions of the arc bounded by the turns) from a particular solution is employed. Thereafter, the turn sequence is updated based on new state information. A primary conclusion from Wawrzyniak and Howell[8] is that the success of the "turn-and-hold" strategy depends on the duration of the subarcs and the number of subarcs used to design a turn sequence, as well as the actuation errors in the reorientation process.

In the present investigation, the turn-and-hold strategy is adapted such that turns do not occur at regular intervals. If the multiple-shooting algorithm fails to converge, the number of turns is increased such that an integer number of days between turns is preserved. The number of turns, and subsequently, the arc length, is increased to some maximum value. If no attempts for a given subarc length converge, the subarc length (i.e., the time between turns) is decreased. Additionally, reference trajectories for this study are developed within the context of an ephemeris model that incorporates solar gravity and lunar pole orientation, as opposed to an idealized Earth–Moon circular restricted three-body (CR3B) model. The adaptive control laws are also developed in the ephemeris model, and are similar to corresponding control laws for the idealized regime. This paper begins with the transition of a reference path generated in an idealized regime to a reference path in an inertial, ephemeris-based regime. Then the mathematical background for modeling solar sail flight-path control is presented, followed by a description and results of the adaptation to the look-ahead turn-and-hold control scheme.

II. Generating a Reference Path in an Inertial, Ephemeris Regime

The advantage of developing trajectories in the Earth–Moon CR3B system is that periodicity is constrained and the resulting orbits are bounded. Terrestrial and lunar gravity, as well as solar radiation pressure but not solar gravity, are incorporated in the force model. A finite-difference method (FDM) approach to the solving the lunar south pole coverage problem using a solar sail spacecraft in that idealized regime is documented in Wawrzyniak and Howell.[9]

The solutions from Wawrzyniak and Howell,[9] however, still require verification. To properly model the motion of the vehicle for a mission scenario, solutions from the simpler model must be transitioned to a higher-fidelity model, such as one based on ephemeris positions and the gravitational effects of the Earth, the Moon, and the Sun.[6] Because the effect of solar gravity on the instantaneous equilibrium surfaces in the Earth–Moon system is minor, a direct transition to an ephemeris-based model and bypassing a bi-circular restricted model that incorporates solar gravity is possible. Additional effects from other solar system bodies may also be included. For the current investigation, the sample trajectories generated in the CR3B regime are used to initialize an FDM process that is based on the ephemeris locations of the Sun, the Earth, and the Moon. The procedure employed to transition the solutions from the Earth–Moon CR3B system to the higher-fidelity model, as well as the results of that transition, are detailed below. Error properties for the FDM scheme discussed in Wawrzyniak and Howell[9] apply to the FDM scheme developed for the inertial, ephemeris model as well. The FDM algorithm is demonstrated to be a viable tool for generating trajectories in high-fidelity models. Two challenges are encountered during an implementation of such a transition. First, the CR3B solution must be transformed into the appropriate path in the inertial frame. Given the new path, it is equally important to formulate an FDM algorithm properly to generate a viable solution.

II.A. Transforming the CR3B solution into an inertial, ephemeris frame

Prior to transitioning a CR3B solution to an ephemeris-based model, an appropriate ephemeris must be selected. For this investigation, the Jet Propulsion Laboratory (JPL) planetary and lunar ephemeris DE 421 is employed, which supplies the orbits of the Sun, planets (including Pluto), and the Moon for the years 1900–2050.[10] This ephemeris is an improvement on previous ephemerides such as the DE 418[11] and the widely used DE 405[10] and is "recommended for lunar missions";[12] lunar ephemerides in the DE 421 ephemeris are available to sub-meter accuracy. However, any of these three ephemerides are sufficient to demonstrate the process.

The ephemerides are loaded into the algorithm using MATLAB®-based SPICE routines, or MICE, available from the JPL Navigation and Ancillary Information Facility (NAIF).[13] Other publicly available

SPICE kernels are also employed in this analysis and are listed in Table 1 in the order in which they are loaded into the MATLAB® environment.[a]

Table 1: SPICE kernels used in the high-fidelity simulation

Kernel	Description
naif0010.tls	Leap second kernel file
pck00010.tpc	General planetary constants kernel (PCK) file
de-403-masses.tpc	GM/mass kernel file (based on DE 403, no update for DE 421)
de421.bsp	Binary planetary and lunar ephemeris
moon_pa_de421_1900-2050.bpc	Binary PCK file for the Moon (lunar orientation, etc.)
moon_080317.tf	Kernel containing lunar frame specifications compatible with moon_pa_de421_1900-2050.bpc

To begin the transformation from the solution in the Earth–Moon CR3B regime into an ephemeris-based model, a date is identified when the Moon is in opposition, for example, 25 July 2029, 13:12:32.239, ephemeris time (ET or $\mathrm{T_{eph}}$),[b] to most closely match the initial conditions of the orbit from the CR3B model. Multiple revolutions from the CR3B orbit are generated by repeating the periodic path for any number of synodic months. Although different characteristic lengths and masses are employed to generate the CR3B trajectories, the distance from the Earth to the Moon, $L^* = 385156.4$ km, is frozen at this value once this date is selected. Additionally, all other reference dimensions and gravitational parameters are obtained from the files appearing in Table 1. Based on *these* dimensions and parameters, the nondimensional path from the CR3B model is dimensionalized and the nondimensional time associated with each state is converted to seconds past the J2000 epoch (1 January 2000, 12:00:00 ET). If appropriate, the states from the reference path can be interpolated.

Rotating the reference path to the ephemeris-based inertial frame employs the instantaneous position and velocity of the Moon with respect to the Earth from the ephemeris data. Let H be the inertial reference frame corresponding to a particular set of ephemerides (i.e., the Earth-mean-equator or Earth-mean-ecliptic at the J2000 epoch) and let $\mathbf{r}^H_{me,i}$ and $\mathbf{v}^H_{me,i}$ be the position and velocity vectors, respectively, of the Earth with respect to the Moon obtained from ephemeris data in this inertial frame at each epoch, t_i, corresponding to the reference path data. A set of unit vectors are constructed based on $\mathbf{r}^H_{me,i}$ and $\mathbf{v}^H_{me,i}$, that is,

$$\hat{\mathbf{X}}^H_i = -\frac{\mathbf{r}^H_{me,i}}{\|\mathbf{r}^H_{me,i}\|}, \quad \hat{\mathbf{Z}}^H_i = \frac{\mathbf{r}^H_{me,i} \times \mathbf{v}^H_{me,i}}{\|\mathbf{r}^H_{me,i} \times \mathbf{v}^H_{me,i}\|}, \quad \hat{\mathbf{Y}}^H_i = \hat{\mathbf{Z}}^H_i \times \hat{\mathbf{X}}^H_i \tag{1}$$

The instantaneous rotation rate vector of the R frame attached to the Earth and the Moon with respect to the H frame is

$$ {}^H\boldsymbol{\omega}^R_i = \frac{\mathbf{r}^H_{me,i} \times \mathbf{v}^H_{me,i}}{\|\mathbf{r}^H_{me,i}\|^2} \tag{2}$$

$$= \frac{\|\mathbf{r}^H_{me,i} \times \mathbf{v}^H_{me,i}\|}{\|\mathbf{r}^H_{me,i}\|^2} \hat{\mathbf{Z}}^H_i \tag{3}$$

Finally, a matrix that rotates a spacecraft state consisting of the position and velocity at t_i from the R frame to the H frame is

$$ {}^H\mathbf{T}^R_i = \begin{bmatrix} \mathbf{C}_i & \mathbf{0} \\ \frac{{}^Hd}{dt}\mathbf{C}_i & \mathbf{C}_i \end{bmatrix} \tag{4}$$

[a] All files are current as of 7 July 2012 and are located in the subdirectories of ftp://naif.jpl.nasa.gov/pub/naif/generic_kernels/.

[b] Curiously, in a cursory trial-and-error search for oppositions, only the opposition on 25 July 2029 and the one occurring on 15 July 2011, 06:15:41.796 ET, lead to successful transitions in the ephemeris model. While other oppositions may exist that lead to a successful transition, the two mentioned here are offset by one Saros cycle.

where the $\frac{^H d}{dt}$ operator indicates a derivative with respect to the H frame and

$$\mathbf{C}_i = \left[\begin{array}{ccc} \hat{\mathbf{X}}_i^H & \hat{\mathbf{Y}}_i^H & \hat{\mathbf{Z}}_i^H \end{array} \right] \tag{5}$$

$$\frac{^H d}{dt}\mathbf{C}_i = \left[\begin{array}{ccc} {}^H\boldsymbol{\omega}_i^R \times \hat{\mathbf{X}}_i^H & {}^H\boldsymbol{\omega}_i^R \times \hat{\mathbf{Y}}_i^H & {}^H\boldsymbol{\omega}_i^R \times \hat{\mathbf{Z}}_i^H \end{array} \right] \tag{6}$$

A rotation from the H frame to the R frame uses the inverse of ${}^H\mathbf{T}_i^R$. An assumption that the Earth, the Moon, and the Sun all lie in the same plane leads to a less accurate initialization of the numerical process (e.g., the FDM algorithm) that is formulated in terms of ephemeris locations of the specified bodies. Therefore, these rotations are necessary because the orientation of the Earth–Moon orbital plane is offset from the ecliptic plane by approximately 5.16°. All vectors highlighted in this section are expressed in the H frame, and, for simplicity, superscript H is dropped from the notation for the remainder of this section.

After rotating the states from the CR3B reference paths to the inertial frame and prior to executing the FDM process to refine those paths based on ephemeris information, the locations of the Sun, the Earth, and the Moon are extracted from the ephemeris file at each epoch, t_i, and the position vectors are re-positioned to originate at a base point at the instantaneous location of the Moon. Additionally, the direction from the center of the Moon to the lunar south pole at each epoch is determined by invoking `cspice_pxform()`. This SPICE function produces a position-based transformation matrix based on the relative orientation of two reference frames. If the arguments into the `cspice_pxform` function are structured so that the result of the `cspice_pxform` operation produces a transformation matrix from an inertial frame to a Moon-fixed body frame, the third column of the matrix is the vector to the lunar north pole. For this application, either a Moon-fixed frame based on the principal lunar inertia axes or a frame based on the north mean lunar rotation axis is employed. The angle between these two frames is 0.02885°, equivalent to approximately 875 m at the lunar poles. In addition to the average 5.16° offset between the Earth–Moon orbital plane and the ecliptic, the angle between the equatorial plane of the Moon and the ecliptic is approximately 1.55°. The angle between the Earth–Moon orbital plane and the equatorial plane of the Moon is approximately 3.85°.

II.B. Formulating the FDM for an ephemeris-based trajectory

The formulation for the FDM algorithm presented in Wawrzyniak and Howell[9] requires only a few significant changes for use in the ephemeris-based inertial frame. The first modification is the change in the constraint equations. The second step in the reformulation of the FDM algorithm is an update of the differential equations that govern motion in the system.

The FDM accommodates both equality and inequality path constraints in both the CR3B formulation and the ephemeris-based formulations (elevation angle and off-sun angle are inequality constraints, while the magnitude of the control vector is constrained to unit length). When the reference trajectories are generated in the CR3B model, the elevation-angle constraint includes a margin to accommodate differences in frame alignment and dynamical characteristics in comparison to an ephemeris-based model. In the high-fidelity formulation, the elevation-angle constraint is relaxed to 9° from 15° in the CR3B formulation. The form of the constraint is generalized to incorporate the correct alignment of the lunar south pole direction as observed from the inertial frame, that is,

$$E_i = \arcsin\left(\frac{\mathbf{r}_{op,i} \cdot \hat{\mathbf{r}}_{mo,i}}{r_{op,i}}\right) \tag{7}$$

$$E_{\min} \leq E_i \tag{8}$$

where E_i is the elevation angle as viewed from the lunar south pole at time t_i, $\mathbf{r}_{mo,i}$ is the vector from the center of the Moon to the lunar south pole, and $\mathbf{r}_{op,i}$ is the vector from the lunar south pole to the vehicle. The minimum elevation angle is $E_{\min}$. These vectors and angles appear in Figure 1. The attitude constraint and the unit magnitude constraint on the control vector remain and are

$$\cos\alpha_{\max} \leq \hat{\boldsymbol{\ell}}_i \cdot \hat{\mathbf{u}}_i \tag{9}$$

$$\mathbf{u}_i^{\mathrm{T}}\mathbf{u}_i = 1 \tag{10}$$

respectively, $\alpha_{\max}$ is the maximum pitch angle allowed between the sail-face normal, $\hat{\mathbf{u}}$, and the vector from the Sun to the sail, $\hat{\boldsymbol{\ell}}$. Normally, $\|\mathbf{u}\| = 1$, but for purposes of the FDM, the values of the components of

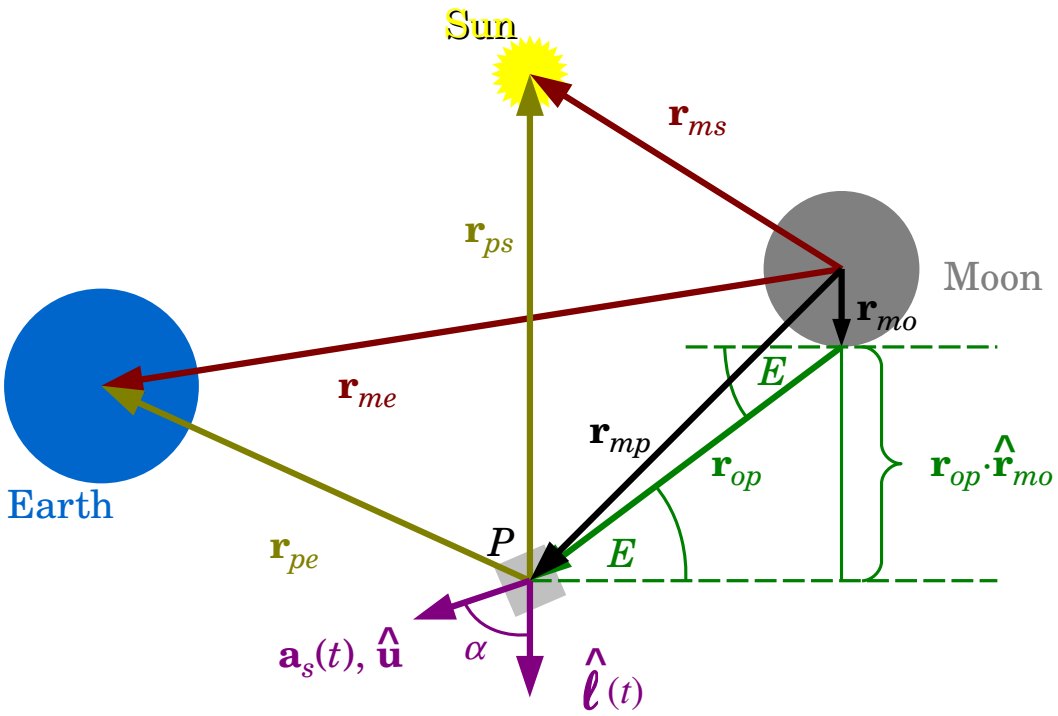

Figure 1: Vectors employed in the Moon-centered equations of motion and vectors for the elevation-angle constraint (in green). The sailcraft is located at point P.

$\mathbf{u}$ are iteratively updated and do not necessarily result in a unit vector until the process converges on an overall solution, requiring $\|\mathbf{u}\| = 1$.[9] (Hereafter, $\hat{\mathbf{u}}$ indicates a sail pointing vector known to be unit length and $\mathbf{u}$ indicates a sail pointing vector not necessarily of unit length.) The value of $\alpha_{\max}$ is always 90° or less if accommodating differences between an ideal solar sail model and a realistic model.[14] The inequality constraints are rewritten as equality constraints that incorporate the associated slack variables, $\eta_{E,i}$ and $\eta_{\alpha,i}$, at each node, that is,

$$\sin E_{\min} - \sin E_i + \eta_{E,i}^2 = 0 \tag{11}$$

$$\cos \alpha_{\max} - \hat{\boldsymbol{\ell}}_i \cdot \hat{\mathbf{u}}_i + \eta_{\alpha,i}^2 = 0 \tag{12}$$

The altitude constraint employed in previous studies is neglected because locations along all of the reference paths are sufficiently close to the Moon for this investigation. Additionally, because the solution is not periodic in the ephemeris-based inertial system, the periodicity constraint is also eliminated.

A new formulation of the equations of motion is also required when searching for trajectories in an ephemeris-based model. To establish this new dynamical model, the Moon is defined as the origin of the coordinate system, and the Sun and the Earth are assumed to move relative to that point. The vector form of the familiar two-body relative equation of motion with perturbations from the gravitational effects due to other celestial bodies,[15–17] as well as the acceleration due to an ideal solar sail, is

$$\ddot{\mathbf{r}}_{mp} + \frac{G(m_p + m_m)}{r_{mp}^3}\mathbf{r}_{mp} = Gm_e\left(\frac{\mathbf{r}_{pe}}{r_{pe}^3} - \frac{\mathbf{r}_{me}}{r_{me}^3}\right) + Gm_s\left(\frac{\mathbf{r}_{ps}}{r_{ps}^3} - \frac{\mathbf{r}_{ms}}{r_{ms}^3}\right) + a_c\left(\frac{\mathrm{AU}}{r_{ps}}\right)^2 \cos^2\alpha\hat{\mathbf{u}} \tag{13}$$

where G is Newton's gravitational constant and m_p is the mass of the sail, which is negligible compared to the mass of the Moon, m_m. The mass of the Earth and the Sun are m_e and m_s, respectively. All vectors in Eq. (13) appear in Figure 1; note that the path is written in terms of $\mathbf{r}_{mp}$ after the transformation to the inertial coordinate frame. Only the point-mass gravitational effects of the Sun, the Earth, and the Moon are

incorporated in the equations of motion in this demonstration. Effects from other bodies, as well as non-spherical perturbations to lunar gravity, are considered negligible. The average gravitational contributions due to the Moon and other possible, significant solar system bodies on a particle moving along a circular path approximately 55000 km from the center of the Moon and offset 15000 km in the $-z$ direction are listed in Table 2 to highlight the relative magnitude of the contributions from the three bodies used in this simulation on the motion of the sail compared to neglected solar system bodies. It is noted that the model is not truly coherent without these additional gravity effects.[a]

Table 2: Average gravitational acceleration contributions from selected solar system bodies on a particle approximately 55000 km from the center of the Moon.

Moon	1.58 mm/s^2	0.568 (nondimensional units)
Earth	0.58 mm/s^2	0.213
Sun	3.24×10^{-3} mm/s^2	1.192×10^{-3}
Lunar J2	2.95×10^{-7} mm/s^2	1.085×10^{-7}
Jupiter	3.61×10^{-8} mm/s^2	1.329×10^{-8}
Venus	1.64×10^{-9} mm/s^2	6.016×10^{-10}

The period of each trajectory is no longer constrained, and an extrapolation of neighboring numerically determined accelerations is employed for calculating the numerical acceleration and the first and last nodes, $\widetilde{\mathbf{a}}_1$ and $\widetilde{\mathbf{a}}_n$, respectively (i.e., $\widetilde{\mathbf{a}}_1$ is a function of positions at the first four nodes, $\mathbf{r}_1$ to $\mathbf{r}_4$, and $\widetilde{\mathbf{a}}_n$ is a function of $\mathbf{r}_{n-3}$ to $\mathbf{r}_n$; $\widetilde{\mathbf{a}}_i$, where $i \neq 1$ or n, is based on the position vectors $\mathbf{r}_{i-1}$, $\mathbf{r}_i$, and $\mathbf{r}_{i+1}$). The tilde in $\widetilde{\mathbf{a}}$ indicates that the acceleration is derived using a finite difference of position vectors. Partial derivatives of these accelerations with respect to position elements at neighboring nodes are tractable analytically for a linear extrapolation of the numerically derived acceleration values at two neighboring nodes.

An important observation concerning the FDM scheme is notable when computing the Jacobian matrix. For the FDM scheme in this high-fidelity simulation, as well as the corrections process in the CR3B simulation, developing the partial derivatives for the Jacobian matrix analytically is generally straightforward; these partial derivatives are often available in a compact form. In the current simulation, $\widetilde{\mathbf{a}}_1$ and $\widetilde{\mathbf{a}}_n$ are extrapolated based on higher-degree polynomials and more node points than those employed for a linear extrapolation. Only in the case where higher-degree polynomials are employed are any partial derivatives, specifically, $\frac{\partial \widetilde{\mathbf{a}}_1}{\partial \mathbf{r}}$ and $\frac{\partial \widetilde{\mathbf{a}}_n}{\partial \mathbf{r}}$, determined by numerical techniques, which increases convergence times compared to formulations based purely on analytically calculated the partial derivatives. In this application, however, the computational cost is not significant and numerically calculating these specific partial derivatives is warranted to improve the accuracy of the solution.

A final pre-processing step is recommended prior to invoking the FDM algorithm, that is, the nondimensionalization of all quantities from the planetary ephemerides and the spacecraft trajectory. With nondimensional quantities, partial derivatives of the accelerations with respect to positions, $\frac{\partial \mathbf{a}}{\partial \mathbf{r}}$, possess orders of magnitudes similar to the corresponding acceleration level. Using dimensional values leads to a poorly conditioned Jacobian matrix, $D\mathbf{F}(\mathbf{X})$, in which the orders of magnitude of the elements corresponding to acceleration terms in the matrix are scaled approximately by a factor of 10^{-6} when compared to a similar nondimensional formulation, and, thus, the algorithm does not converge on a solution when using dimensional values.

II.C. Sample trajectories transitioned to an ephemeris-based regime

One advantage of developing trajectories within the context of the Earth–Moon CR3B regime is that the model incorporates the dominant gravitational contributions from the Earth and the Moon as well as the effect of solar radiation pressure on the sailcraft. The use of this framework reflects an assumption that this idealized CR3B system is a reasonable simplification of a higher-fidelity model. One such model, described in the previous subsection, is based on the ephemeris positions of the Earth and the Moon as well as solar

[a]Russell reminds his readers of the importance of incorporating all of the dominant perturbing bodies present in the generation of the ephemeris to avoid "ghost" accelerations in high-fidelity simulations.[18] The authors acknowledge this fact and note it for future development.

ephemeris positions and solar gravity. A test of the utility of the CR3B assumption is to use a solution developed in that regime to initialize a trajectory generation process in a higher-fidelity model such that the resulting high-fidelity solution resembles the original CR3B solution.

Both of the sample orbits used in Wawrzyniak and Howell[8] (depicted in Figure 2) are employed successfully to generate new trajectories based on an ephemeris model. In the Moon-centered inertial frame, the

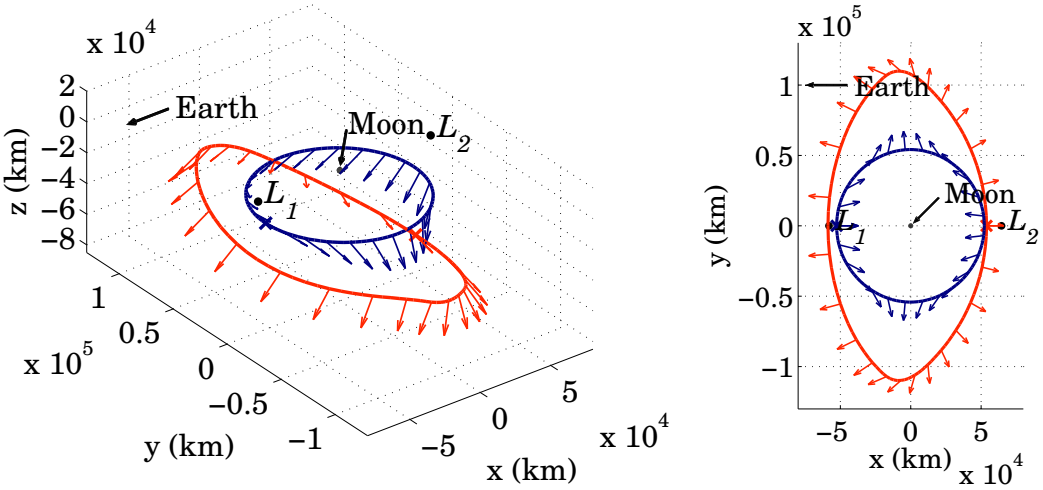

(a) 3-D view (b) xy view

Figure 2: Two sample reference trajectories below the Moon generated in a CR3B regime. The arrows represent the direction of the sail-face normal.

resulting orbits appear in Figure 3. The directions to the Sun and the Earth are initially toward the upper left in Figure 3(b). Note that the dark-blue orbit completes two cycles in the inertial frame in one month, while the red-orange orbit requires one year to complete a revolution about the Moon. For comparison to the CR3B initializing orbits, the inverse of ${}^{H}\mathbf{T}_{i}^{R}$ from Eq. (4) is used on the inertially defined trajectory at each epoch, and the results from the FDM scheme are transformed into a Moon-centered rotating frame that is based on the instantaneous position and velocity of the Earth with respect to the Moon. Results for a one-month simulation initiating on 25 July 2029, 13:12:32.239 ET, appear in Figure 4, along with the

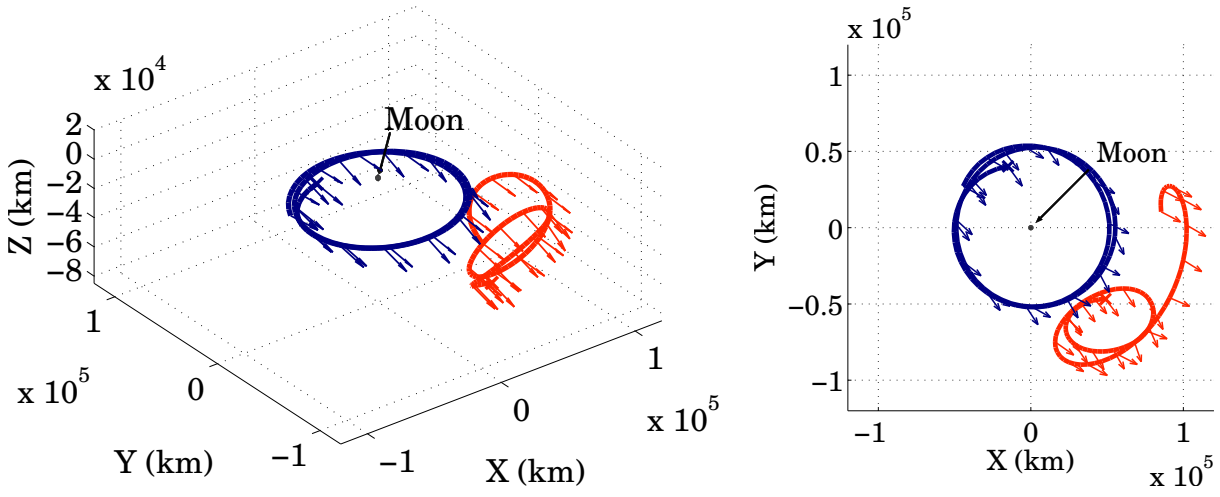

(a) 3-D view (b) xy view

Figure 3: Two sample reference trajectories below the Moon transitioned from a CR3B regime to an ephemeris-based regime and depicted in the Moon-centered inertial frame. The arrows represent the direction of the sail-face normal.

elevation-angle profile of the trajectory as viewed from the lunar south pole. The locations of L_1 and L_2 from the CR3B formulation are included in the figure for a comparison of the ephemeris-based results to their corresponding solutions in the CR3B model. Note that the locations of L_1 and L_2 are instantaneous in the Moon-centered rotating frame. Because periodicity is not constrained, the orbits in Figure 2 do not close during the one-month simulation. An "x" marks the position of the spacecraft at this initial epoch along each trajectory.

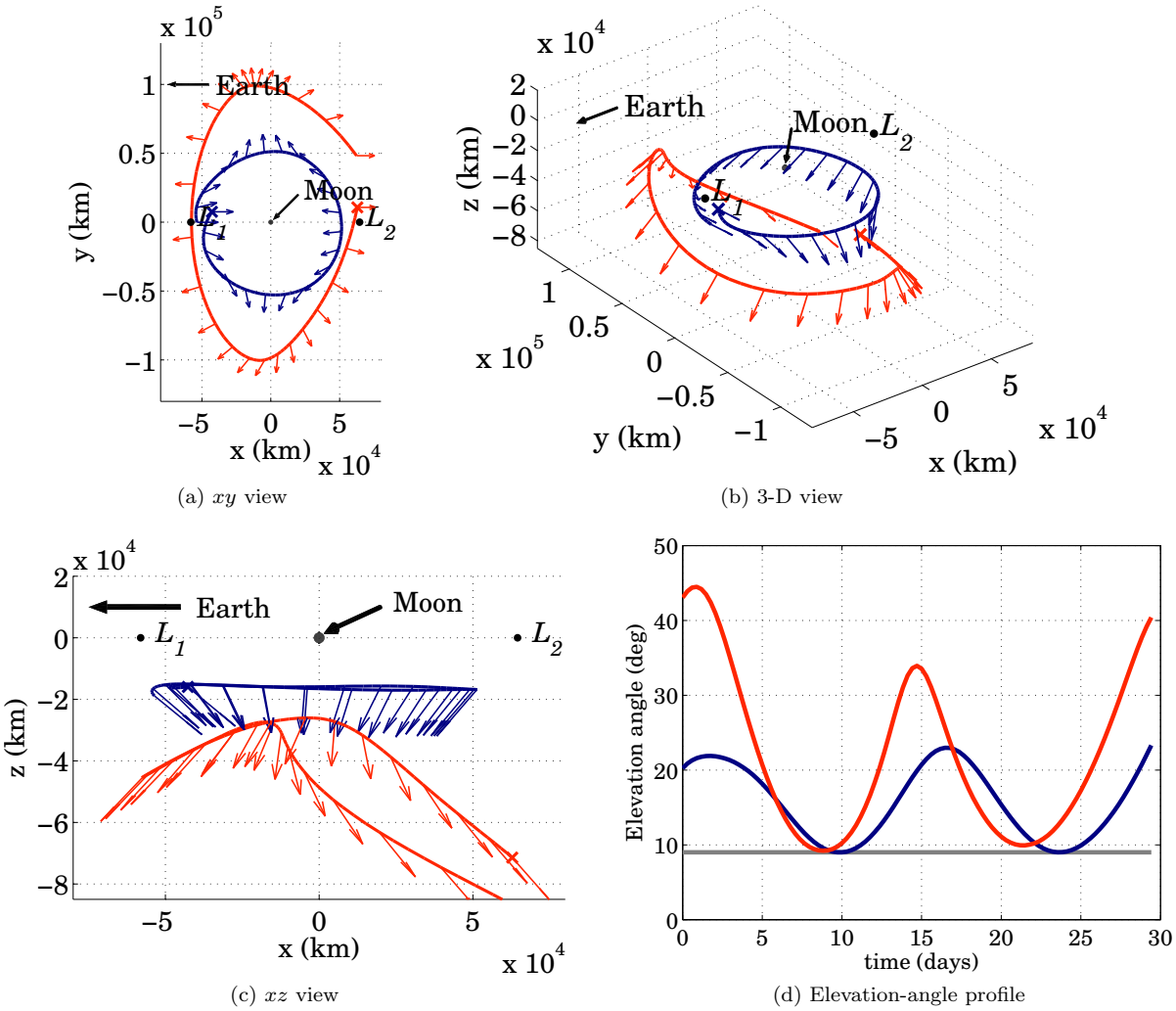

(a) xy view

(b) 3-D view

(c) xz view

(d) Elevation-angle profile

Figure 4: Three views of a one-month simulation of two sample trajectories as viewed relative to a Moon-centered rotating frame (*cf.* Fig 2) along with the associated elevation-angle profile. The gray line in (d) represents the 9° minimum elevation-angle requirement.

The FDM algorithm is adaptable for any simulation length. Results from a twelve-month simulation appear in Figures 5 and 6 (the arrow representing the sail-face normal are removed for clarity). One immediate observation from a longer simulation involves the first and last revolutions. These "bounding" revolutions possess segments that extend beyond the quasi-periodic region that defines the balance of the trajectory, even when a more accurate numerical model for the acceleration components is incorporated at the first and the last nodes in the FDM algorithm. It is common practice to include an extra revolution prior to and beyond the time of interest for a simulation when the first and last points are unconstrained, then to discard those revolutions as superfluous to a high-fidelity reference path. The algorithm uses those initial and final locations to increase flexibility, and transfer trajectories are linked to locations along the reference path interior to these nodes.

Further improvement in model fidelity is possible. Effects from additional solar system bodies are easily incorporated into the differential equations and subsequent partial derivatives of the finite-difference method.

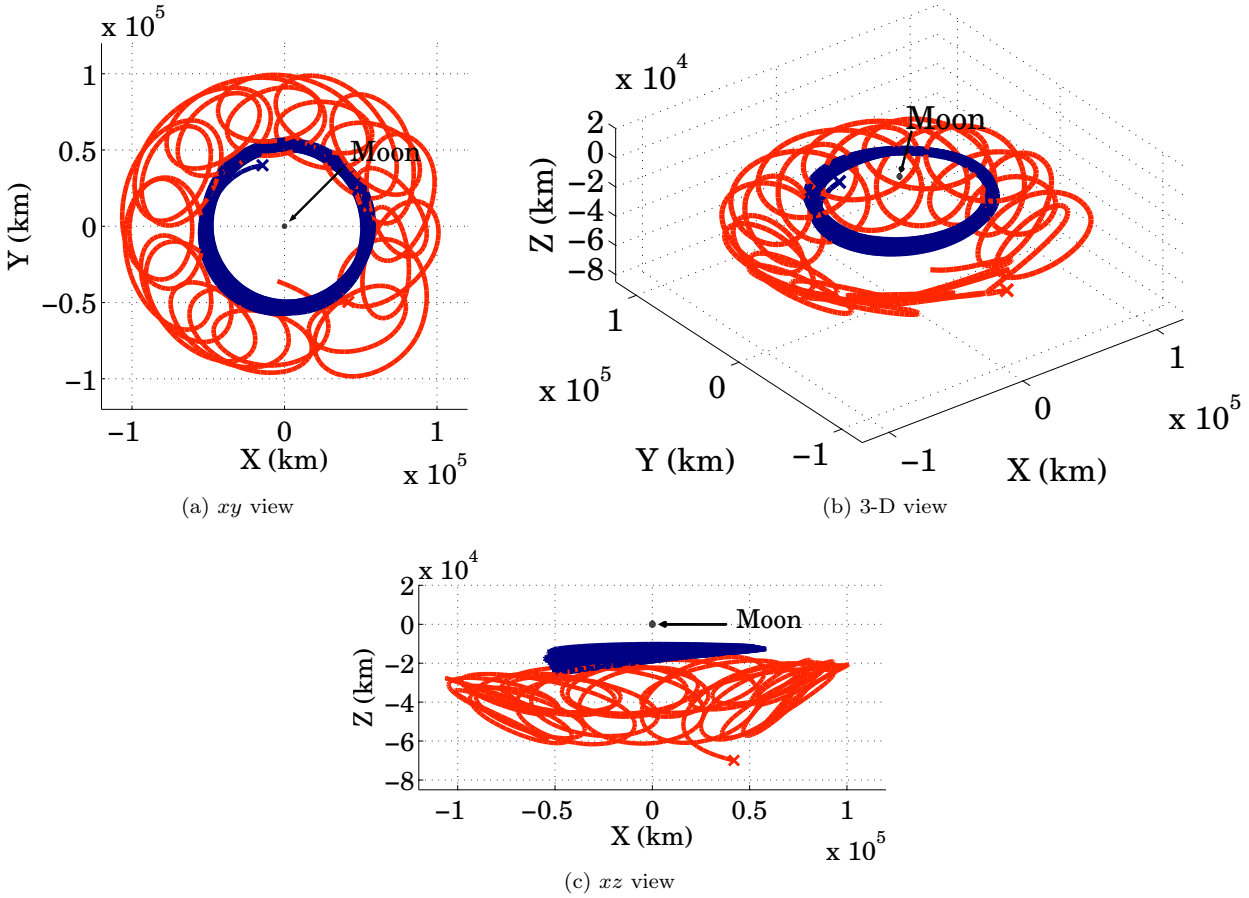

(a) xy view

(b) 3-D view

(c) xz view

Figure 5: Twelve-month simulation of two sample trajectories as viewed in a Moon-centered inertial frame.

However, prior experience suggests that these effects are minor in comparison to improvements in the sail reflectivity model and the incorporation of disturbances due to lunar and terrestrial spherical harmonics. An optical model represents the next level of fidelity in the spacecraft model.[19] Further improvements to the solar sail reflectivity model incorporate sail deformation and manufacturing defects.[14,19,20] Additionally, higher-fidelity numerical methods improve the numerical precision of the solution.[6,21,22] The solutions from this ephemeris model demonstrate that the FDM algorithm is useful for improving the accuracy of lower-fidelity solutions. Despite the accuracy or precision employed in the determination of a reference trajectory, however, the flight path of a spacecraft following that reference orbit must be controlled.

III. Mathematical Modeling for Solar Sail Flight-Path Control

Designing reference trajectories and understanding the fundamental dynamics are necessary first steps toward flying sailcraft in dynamically complicated regimes, such as an environment simultaneously influenced by the gravity of multiple bodies. However, the existence of a reference orbit alone is insufficient for flight. The spacecraft must be controlled to follow the reference path. Regardless of the accuracy attained for a trajectory arc, or the precision of the numerical method employed, no spacecraft exactly follows the intended path. Model uncertainty, mis-modeling, and model fidelity associated with both the space vehicle and its environment all contribute to perturb the spacecraft trajectory. Furthermore, unless the equations of motion are analytically solvable, any numerical strategy is limited and only solves the equations of motion approximately. When the orbit is unstable, which is true for an offset lunar solar sail orbit as determined in this investigation, the sailcraft must be controlled to follow the reference path; otherwise, a slight deviation from the path often leads to a trajectory that rapidly diverges from the desired course.

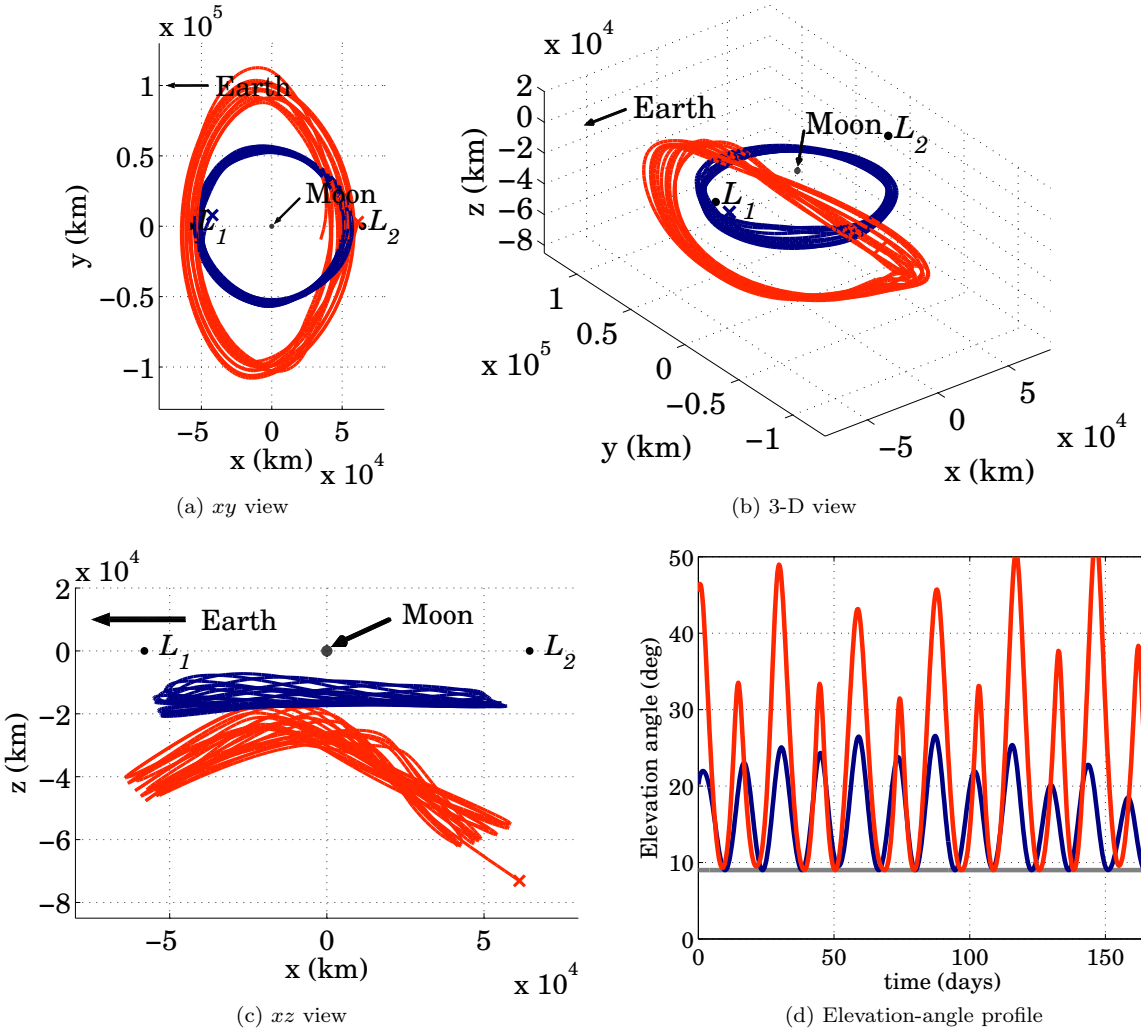

(a) xy view

(b) 3-D view

(c) xz view

(d) Elevation-angle profile

Figure 6: Three views of a twelve-month simulation of two sample trajectories as viewed relative to a Moon-centered rotating frame along with the associated elevation-angle profile. The gray line in (d) represents the 9° minimum elevation-angle requirement.

Previous studies by Wawrzyniak and Howell[8, 23] establish that a "turn-and-hold" strategy is successful in controlling the flight-path for the vehicle. In this strategy, the attitude of the sailcraft is inertially fixed for some duration and then turned to a new orientation such that the vehicle follows the reference trajectory. In Wawrzyniak and Howell,[8] a multiple-shooting scheme is employed to correct an initial guess for the inertially fixed attitude necessary for the vehicle follows the reference trajectory. The foundations for the present study are based on the formulation for the turn-and-hold strategy presented in Wawrzyniak and Howell[8] and is repeated here for completeness.

The definitions of terms used in this investigation are specified for clarity. A future state along the reference path is selected as a *target*. The portion of the trajectory between the present state and the target is called an *arc*. An arc may be decomposed into one or more *segments* or *subarcs*, where the boundaries of a subarc occur when a turn is executed. Thus, the length of an arc is the number of turns (segments or subarcs) multiplied by the time between turns. The length of a subarc is measured by the length of time between the turns that define its boundaries. The time at which a turn is executed is denoted an *event*. Because the reference paths from the FDM are reported at discrete intervals, an Akima cubic-spline[24] is employed to interpolate the reference attitude profile. The set of orientations, as well as their associated event times, necessary to achieve the target state at the end of the arc is labeled a turn *sequence* or *profile*.

Along a particular subarc, the sail attitude is fixed (as a consequence, the attitude is time-varying along the entire arc segment in a rotating Earth–Moon frame). The attitude can be expressed in terms of latitude, ϕ_i, and longitude, θ_i, angles for subarc i. For convenience, $\phi_i \equiv \phi(t_i)$ and $\theta_i \equiv \theta(t_i)$. The initial guess for the latitude, ϕ_i^0, and the longitude, θ_i^0, corresponding to each subarc are the average values from the continuous values of ϕ and θ generated over arc segment i from the reference solution. The average is calculated based on the values of ϕ and θ at t_i and t_{i+1}, that is,

$$\phi_i^0 = \frac{\phi(t_{i+1}) + \phi(t_i)}{t_{i+1} - t_i} \tag{14a}$$

$$\theta_i^0 = \frac{\theta(t_{i+1}) + \theta(t_i)}{t_{i+1} - t_i} \tag{14b}$$

The sail pointing vector is expanded in terms of spherical coordinates in an inertial frame, that is,

$$\hat{\mathbf{u}}_i = u_{X,i}\hat{\mathbf{X}} + u_{Y,i}\hat{\mathbf{Y}} + u_{Z,i}\hat{\mathbf{Z}} \tag{15a}$$

$$= \cos\phi_i \cos\theta_i \hat{\mathbf{X}} + \cos\phi_i \sin\theta_i \hat{\mathbf{Y}} + \sin\phi_i \hat{\mathbf{Z}} \tag{15b}$$

Like the reference path, the reference attitude profile from the FDM solution is reported at discrete time intervals that are not necessarily coincident with the epoch associated with a turn. Again, an Akima cubic spline[24] is employed to interpolate the reference attitude profile.

To initialize the multiple-shooting scheme, the trajectory and a state transition matrix are numerically propagated from one epoch to the next using an explicit integration scheme, as illustrated in Figure 7. The state at t_{i+1} resulting from the integration is labeled $\mathbf{x}_{i+1}(\mathbf{x}_i, \hat{\mathbf{u}}_i)$ because it is initialized with $\mathbf{x}_i$ and $\hat{\mathbf{u}}_i$. These propagated trajectories are the subarcs and almost always diverge from their intended targets. When the subarcs are connected, they form the arc. In Figure 7, the black curve represents the reference path and the red curves reflect the actual path of the propagated trajectory with an initial set of fixed attitude angles, integrated from one epoch to the next for h epochs and using initial conditions extracted from the reference path. The difference between the state propagated from one epoch to the next and the state extracted from the reference path at that next epoch forms the basis for a multiple-shooting corrections process.

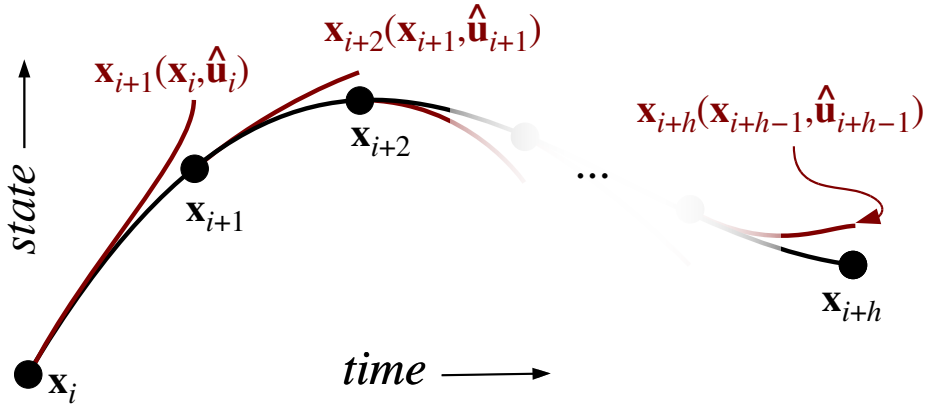

Figure 7: Example of propagated subarcs (red) extracted from a reference path (black). The arc is defined from t_i to t_h. The first subarc occurs between t_i and t_{i+1}.

The aim of using multiple shooting for this application is to develop a continuous path from $\mathbf{x}_i$ to $\mathbf{x}_{i+h}$ by adjusting the control parameters, $\mathbf{u}_i$, $\mathbf{u}_{i+1}$, ..., $\mathbf{u}_{i+h}$,[a] and the intermediate states, $\mathbf{x}_{i+1}$, $\mathbf{x}_{i+2}$, ..., $\mathbf{x}_{i+h-1}$. Similar to the path constraints introduced for the FDM in Wawrzyniak and Howell,[7,9] path constraints may also be incorporated into a multiple-shooting scheme. The only required path constraint for a solar sail trajectory is the pitch-angle constraint, where $\alpha \leq \alpha_{\max}$ and $\alpha_{\max}$ is no greater than 90°. This inequality constraint is implemented via a slack variable, η_α. A second path constraint for the elevation angle, where $E \geq E_{\min}$, is similarly implemented via a slack variable, η_E. These slack variables are determined

[a]Recall that $\mathbf{u}$ is only unit length for initial guesses and converged solutions.

in conjunction with the control variables and the intermediate states.[a] Other inequality path constraints may be similarly implemented. This investigation assumes that tracking a reference trajectory that already conforms to the specified path constraints is sufficient and minor incursions into constrained regions at times not coinciding with reorientation events is allowable. A vector comprising the control and slack variables, as well as the intermediate states, is written as

$$\mathbf{X} = \left\{ \mathbf{u}_i \;\; \eta_{\alpha,i} \;\; \mathbf{x}_{i+1} \;\; \eta_{E,i+1} \;\; \mathbf{u}_{i+1} \;\; \eta_{\alpha,i+1} \;\; \ldots \;\; \mathbf{x}_{i+h-1} \;\; \eta_{E,i+h-1} \;\; \mathbf{u}_{i+h-1} \;\; \eta_{\alpha,i+h-1} \right\}^{\mathrm{T}} \tag{16}$$

Note that the control vector at the beginning of the arc, $\mathbf{u}_i$, may be adjusted, but the initial position and velocity, $\mathbf{x}_i$, are fixed. Consequently, the slack variable associated with the pitch-angle constraint is applied at t_i. Also, the control vectors in Eq. (16) are guaranteed to be unit length only when $\mathbf{X}$ represents an initial guess or a converged solution and not necessarily at any other iteration during the numerical solution process.

The elements in $\mathbf{X}$ are used to satisfy a vector equation such that all elements are theoretically zero for a converged solution. For this lunar south pole application, this vector is represented as

$$\mathbf{F}(\mathbf{X}) = \left\{ \begin{array}{c} \mathbf{u}_i^{\mathrm{T}}\mathbf{u}_i - 1 \\ \cos\alpha_{\max} - (\hat{\boldsymbol{\ell}}_i \cdot \mathbf{u}_i) + \eta_{\alpha,i}^2 \\ \mathbf{x}_{i+1}(\mathbf{x}_i, \mathbf{u}_i) - \mathbf{x}_{i+1} \\ \sin E_{\min} + \frac{z_{i+1}+R_m}{A_{i+1}} + \eta_{E,i+1}^2 \\ \vdots \\ \mathbf{u}_{i+h-1}^{\mathrm{T}}\mathbf{u}_{i+h-1} - 1 \\ \cos\alpha_{\max} - (\hat{\boldsymbol{\ell}}_{i+h-1} \cdot \mathbf{u}_{i+h-1}) + \eta_{\alpha,i+h-1}^2 \\ \mathbf{x}_{i+h}(\mathbf{x}_{i+h-1}, \mathbf{u}_{i+h-1}) - \mathbf{x}_{i+h} \end{array} \right\} = \mathbf{0} \tag{17}$$

The constraint $\mathbf{u}_i^{\mathrm{T}}\mathbf{u}_i - 1 = 0$ ensures that the control vector is unit length at the first epoch (similar constraints are employed for the remaining epochs).[b] An elevation-angle constraint is applied, but only to the intermediate states. Recall that the target state is extracted from the reference trajectory; therefore, the elevation-angle constraint is already satisfied at the end points. Because the algorithm is targeting the state at t_{i+h} and the state is fixed at t_i, an elevation-angle constraint at these end points would be either redundant or possibly inconsistent.

An alternative (or supplement) to the elevation-angle constraint is a distance restriction to limit the excursion from the reference path at points along the trajectory. To prevent singularities in the partial derivatives of the distance restriction with respect to position variables, the square of the distance is employed in formulating the constraint, that is,

$$d^2 \leq d_{\max}^2 \tag{18}$$

Similar to the other path constraints, this inequality constraint is imposed via a slack variable, η_d, resulting in an equality constraint,

$$d^2 - d_{\max}^2 + \eta_d^2 = 0 \tag{19}$$

Like the elevation-angle constraint, this distance constraint is only applied to the intermediate states.

The elements in Eq. (17) are not equal to zero initially. The nonlinear dependence of this targeting constraint on a set of control parameters is approximated with a Taylor expansion; higher-order terms are neglected. The expansion is rearranged such that the Jacobian relating the partial derivatives of the constraints, $\mathbf{F}(\mathbf{X}^j)$, with respect to the control variables, $\mathbf{X}^j$, from Eqs. (16) and (17), undergoes a pseudo-inverse that maps errors in the elements in $\mathbf{F}$ to a set of corrections to $\mathbf{X}$, that is,

$$\delta\mathbf{X} = -\left[\frac{\partial\mathbf{F}(\mathbf{X}^j)}{\partial\mathbf{X}^j}\right]^{+} \mathbf{F}(\mathbf{X}^j) \tag{20}$$

[a] In the current formulation, the path constraints only apply at times coincident with the intermediate states (the pitch-angle constraint is also applied at t_i). These constraints may be applied anywhere, including at other epochs between the intermediate states. However, additional path constraints anywhere along the orbit may impede convergence.

[b] A formulation that employs two angles to represent the attitude (obviating the unit length constraint) is not successful.

where j is the iteration index. Those corrections are applied to the next iteration of the state vector, i.e.,

$$\mathbf{X}^{j+1} = \mathbf{X}^{j} + \delta\mathbf{X} \tag{21}$$

Because the number of elements in $\mathbf{X}$ exceeds the number of elements in $\mathbf{F}$ (i.e., the Jacobian contains more columns than rows), the problem is under-constrained and an infinite number of solutions to Eq. (20) exist. A minimum-norm update is employed in a differential-corrections process for the pseudo-inverse in Eq. (20). Dropping i for convenience, the Jacobian is evaluated from the form

$$\frac{\partial \mathbf{F}(\mathbf{X})}{\partial \mathbf{X}} = \begin{bmatrix}
2\mathbf{u}_0^{\mathrm{T}} & & & & & & & & & & \\
\hat{\boldsymbol{\ell}}_0^{\mathrm{T}} & 2\eta_{\alpha,0} & & & & & & & & & \\
\boldsymbol{\Psi}_{1,0} & 0 & -\mathbf{I} & & & & & & & & \\
 & & \boldsymbol{\Gamma}_1 & 2\eta_{E,1} & & & & & & & \\
 & & \mathbf{0} & 0 & 2\mathbf{u}_1^{\mathrm{T}} & & & & & & \\
 & & \mathbf{0} & 0 & \hat{\boldsymbol{\ell}}_1^{\mathrm{T}} & 2\eta_{\alpha,1} & & & & & \\
 & & \boldsymbol{\Phi}_{2,1} & 0 & \boldsymbol{\Psi}_{2,1} & 0 & -\mathbf{I} & & & & \\
 & & & & & & \boldsymbol{\Gamma}_2 & 2\eta_{E,2} & & & \\
 & & & & & & & & \ddots & & \\
 & & & & & & & & -\mathbf{I} & & \\
 & & & & & & & & \boldsymbol{\Gamma}_{h-1} & 2\eta_{E,h-1} & \\
 & & & & & & & & \mathbf{0} & 0 & 2\mathbf{u}_{h-1}^{\mathrm{T}} \\
 & & & & & & & & \mathbf{0} & 0 & \hat{\boldsymbol{\ell}}_{h-1}^{\mathrm{T}} \quad 2\eta_{\alpha,h-1} \\
 & & & & & & & & \boldsymbol{\Phi}_{h,h-1} & 0 & \boldsymbol{\Psi}_{h,h-1} \quad 0
\end{bmatrix} \tag{22}$$

where $\mathbf{u}_0$ is the inertially defined three-element sail-face normal vector from Eq. (15) at time t_{i+0}. The control parameters in Eqs. (16) and (22) are defined with respect to the inertial frame (i.e., Eq. (15)). The matrix $\mathbf{0}$ is a one-by-six array of zeros, $\mathbf{I}$ is the six-by-six identity matrix, and $\boldsymbol{\Phi}_{1,0}$ is the state transition matrix from t_{i+0} to t_{i+1}. The state-control transition matrix from t_{i+0} to t_{i+1}, $\boldsymbol{\Psi}_{1,0}$, is developed from the partial derivatives of the sail acceleration in Eq. (13) with respect to the components of the control vector, that is,

$$\boldsymbol{\Psi}_{1,0} = \frac{\partial \mathbf{a}_{\mathbf{s}}(t)}{\partial \mathbf{u}} = \begin{bmatrix}
0 & 0 & 0 \\
0 & 0 & 0 \\
0 & 0 & 0 \\
\frac{\partial a_{x,1}}{\partial u_{X,0}} & \frac{\partial a_{x,1}}{\partial u_{Y,0}} & \frac{\partial a_{x,1}}{\partial u_{Z,0}} \\
\frac{\partial a_{y,1}}{\partial u_{X,0}} & \frac{\partial a_{y,1}}{\partial u_{Y,0}} & \frac{\partial a_{y,1}}{\partial u_{Z,0}} \\
\frac{\partial a_{z,1}}{\partial u_{X,0}} & \frac{\partial a_{z,1}}{\partial u_{Y,0}} & \frac{\partial a_{z,1}}{\partial u_{Z,0}}
\end{bmatrix} \tag{23}$$

Finally, the partial derivatives of the elevation-angle constraint with respect to the position coordinates are collected in the matrix $\boldsymbol{\Gamma}$. If the distance restriction is employed in lieu of the elevation-angle constraint, then the partial derivatives of the distance restriction with respect to the position components replaces $\boldsymbol{\Gamma}$ and η_d substitutes for η_E.

Propagations that employ information from these new states and updated attitudes supplied by Eq. (20) and (21) are used to repeat the process. A series of iterations proceeds until a convergence tolerance is satisfied (or some stopping condition is triggered), and a continuous trajectory emerges from t_i to t_{i+h}, where the vehicle is reoriented at each epoch.

For any iterative process, convergence is not guaranteed, even in the presence of a supposedly "good" initial guess. However, for the cases examined in this investigation, a good initial guess originating from the reference trajectories generated by the FDM is sufficient to initialize a control scheme that allows the spacecraft to track the corresponding reference trajectory.

IV. Adaptive control with simulated errors

In the study by Wawrzyniak and Howell,[8] a look-ahead strategy, whereby the first turn in a sequence is executed and then the turn sequence is re-initialized, is developed to deal with control, orbit-determination,

and modeling errors. The strategy employs a fixed number of days between turns and a fixed number of turns used in developing the sequence. Extending the work from that investigation, an alternative strategy to track a reference trajectory is examined. To generate a turn sequence, assume that the subarc length and the number of turns employed are adaptable. This "adaptive" scheme is similar to the look-ahead strategy, in that only the first turn-and-hold subarc from a particular solution is employed.

For this investigation, it is convenient to schedule turns at an integer number of days, preferably separated by multiple days. It also is desirable to maintain the flight path close to the reference orbit over the first subarc. These two objectives are sometimes in conflict. For this flight-path control strategy, a given subarc length and a given number of turns are initially employed to generate a turn sequence. If the multiple-shooting algorithm fails to converge, the number of turns is increased such that an integer number of days between turns is preserved. The number of turns, and subsequently, the arc length, is increased to some maximum value. If no attempts for a given subarc length converge, the subarc length (i.e., the time between turns) is decreased. A sample strategy that initially employs a combination of four days between turns and three subarcs appears in Figure 8. In this example, three turns are initially spaced four days apart.[a] If

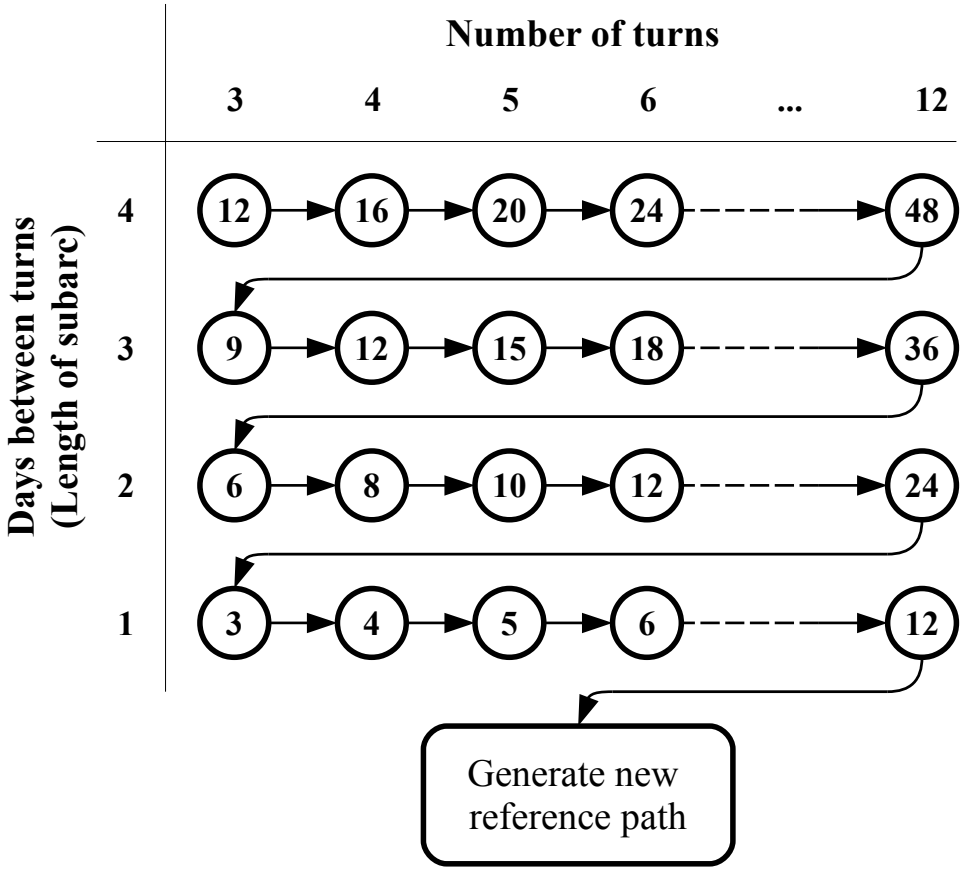

Figure 8: Map of adaptive strategy. The circled number indicates the arc length in days and the arrows point to the next combination of subarc lengths and number of turns to attempt if the current combination fails.

the initial combination does not result in convergence of the algorithm to an acceptable trajectory, another turn is added. To add a turn and maintain the same time interval between turns, the length of the arc is increased until a limit for the number of turns is reached (12 turns in this example). Then, the subarc length decreases to three days. Alternative formulations are initiated with three or two days between turns (i.e., starting on the second or third row of the grid in Figure 8). Consistent with the previous implementation of the look-ahead method, a new turn profile is generated after each subarc.

[a]Note that at least three turns are required to ensure that the number of control variables (two angles per turn) is equal to or greater than the number of target states (position and velocity components) at the target state at the end of an arc.

Two different strategies are examined for the adaptive tracking scheme. The first employs an elevation-angle constraint. Because the simulated flight of the spacecraft could diverge from the reference path, but remain within the elevation-angle constraint, a second strategy employs an excursion constraint at the turn events when designing the turn sequence. Recall that these separate constraints are only applied at the time of the turns and nowhere else along the subarc. While more turns implies more constraints, the algorithm may be more likely to converge in the presence of more control variables. In scenarios to test both strategies, a fourteen-month reference trajectory is generated and the spacecraft must follow the path from the middle of the first month to the middle of the last month. Random errors in the knowledge of the state are 10 km in position and 10 cm/sec in velocity (3σ) at the beginning of the arc, with a 3σ random turn execution error of 1°. The simulations also incorporate a 10°/hr turn that is not included when designing the turn sequence, which assumes instantaneous turns. The results for these two strategies employing initial turn spacings of four, three, and two days for each of the sample orbits are summarized in Table 3. Note that g indicates the

Table 3: Adaptive targeting: 1° control error (3σ) with state knowledge of 10 km in position and 10 cm/sec in velocity (3σ) and 10°/hr slew rates

Color	red-orange			dark-blue		
Initial Window, g_0 (days)	4	3	2	4	3	2
7° elevation-angle constraint						
Trial	A	B	C	D	E	F
Max Excur. (km)	10192	9280	3991	5461	5297	1786
Min Elev. Angle	8.98°	8.83°	9.33°	11.96°	11.51°	11.81°
No. of revs.	13	13	13	3	1	0
Ave. g (days)	3.85	2.94	1.97	3.75	3.00	1.90
Ave. h (turns)	3.40	3.65	4.24	3.11	3.27	3.80
5000 km excursion constraint						
Trial	G	H	I	J	K	L
Max Excur. (km)	7483	6299	3415	5861	5293	3556
Min Elev. Angle	10.26°	9.20°	9.24°	8.55°	9.47°	8.85°
No. of revs.	1	13	13	6	6	13
Ave. g (days)	3.92	2.99	2.00	3.79	2.96	2.00
Ave. h (turns)	4.00	3.63	4.03	3.58	3.39	3.40

subarc length (or days between turns), g_0 is the initial subarc length employed in the adaptive scheme, and h is the number of turns used to generate the turn-and-hold profile. For these cases, most subarc lengths that result in converged solutions for the controlled fight path are equivalent to the initial subarc length, as indicated by the fact that the average value for g is slightly lower than g_0. Additionally, the average number of turns, h, successfully employed to generate a turn sequence is generally below five turns. When the initial subarc length for the time between turns is large (e.g., $g = 4$ days), large excursions from the reference path result. It is interesting to note that the elevation-angle constraint is not activated in scenarios A through F. The minimum elevation angle for the elevation-angle-constrained, dark-blue trajectories (scenarios D through F) is above 11°, but the number of complete revolutions prior to failure of the controller is small. Trajectories from scenarios A through L are visibly similar to those appearing in Figures 4 and 5 (except that they are generated over a slightly different time span). Sample elevation-angle and excursion profiles from scenarios A and L appear in Figure 9. The 7° elevation-angle constraint applied in scenario A is represented by a dashed red line in the top plot, and the 5000-km distance applied in scenario L is represented by a dashed line in the bottom plot.

It may appear from Table 3 that the red-orange orbit is more suited to the adaptive controller. However, because the applied errors are Gaussian random variables, different trials produce different results. A Monte Carlo simulation prior to mission implementation is required. As discussed previously, control errors affect the ability of a flight-path control algorithm to track a reference trajectory successfully. Results from (1) adaptive tracking schemes that incorporate no orbit determination errors, no control errors, and no turn modeling errors along with (2) similar schemes that incorporate 3σ random errors of 10 km in position

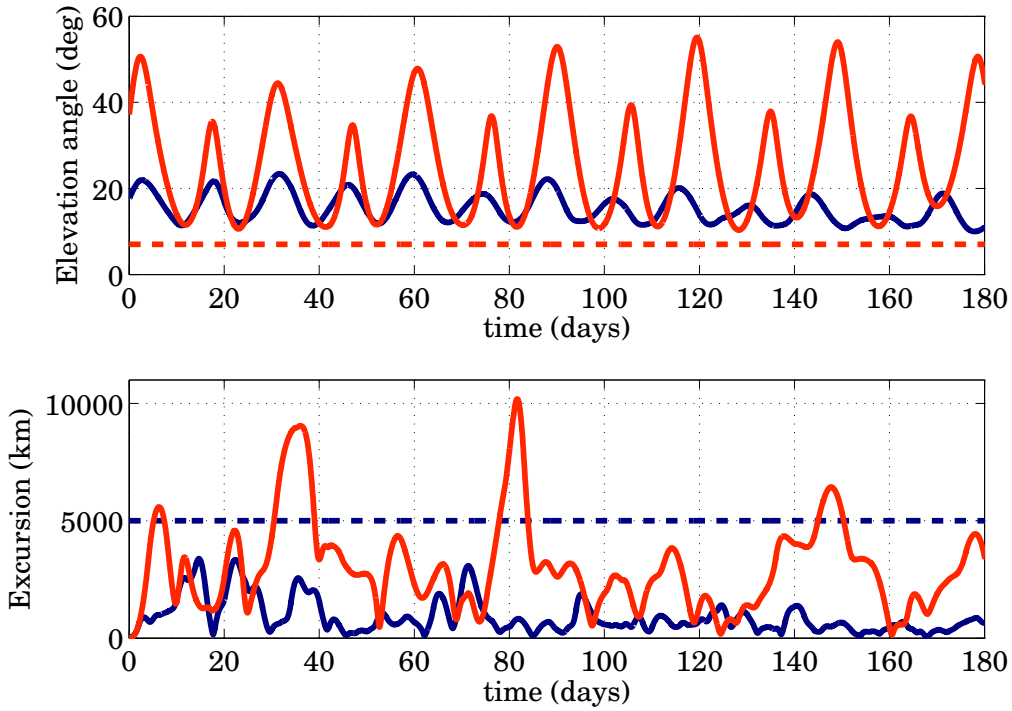

Figure 9: Elevation-angle and excursion profiles for scenarios A (red) and L (blue), corresponding to 1° errors in control.

and 10 cm/s in velocity, as well as 10°/hr slew rates (instantaneous turns are assumed in the design of the sequence) and 3° control errors (as opposed to the 1° control errors examined previously in Table 3), appear in Tables 4 and 5, respectively. Even in the error-free cases, the adaptive scheme employing an elevation-angle constraints exhibits difficulty in tracking some reference trajectories; presumably, the partially bounded trajectory diverges too far from the reference path for the adaptive controller to generate a solution. However, some orbits can be tracked in the presence of large control errors (3°, 3σ), even in the presence of the standard state knowledge and turn modeling errors. These results indicate that path constraints between the re-orientation events (i.e., the times of the turns) may be required if longer times between turns are desired, especially if pointing errors are large.

Any turn-and-hold scheme applied to these reference trajectories is essentially a hybrid control system where a discrete control law is applied to a continuous system. In practice, an upper limit on the time between turns will exist, independent of any number of path constraints. More trials involving various sizes of the excursion constraint may improve the performance of the algorithm. Alternatively, an approach that adds path constraints on the velocity vector (such as a cone constraint or a magnitude constraint) may improve the ability of the adaptive scheme to track a reference path. The adaptive tracking scheme, in the presence of large control errors, can successfully track a sailcraft trajectory and warrants further investigation.

V. Conclusions

Two of the challenges associated with flight-path control for a solar sail vehicle involve the thrusting mechanism (i.e., the sail). The thrust control is (1) effectively always "on" (a feature exploited in this investigation for producing displaced, non-Keplerian orbits) and (2) only supplies two degrees of control for the trajectory: thrust magnitude is a function of attitude. One control solution is continuous reorientation of the vehicle, but this strategy is difficult in practice. An alternative control option is completion of at least three discrete turns to achieve a six-element target state. A multiple-shooting approach is employed to generate the necessary turns in a turn profile, while subjecting the resulting trajectory and sail attitude to the necessary path constraints.

Errors in orbit knowledge and sail attitude control implementation, as well as the fidelity of the slew modeling, are persistent in any sail application, and a controlled flight path will diverge from its intended

Table 4: Adaptive targeting: no errors in control and orbit-determination knowledge and instantaneous slew rates

Color	red-orange			dark-blue		
Initial Window, g_0 (days)	4	3	2	4	3	2
7° elevation-angle constraint						
Trial	A	B	C	D	E	F
Max Excur. (km)	8759	7400	2338	19836	5804	1232
Min Elev. Angle	9.50°	9.32°	10.99°	7.48°	8.85°	11.36°
No. of revs.	13	13	3	12	13	5
Ave. g (days)	3.85	2.94	1.84	3.78	2.83	1.97
Ave. h (turns)	3.35	3.44	3.98	3.09	3.09	3.19
5000 km excursion constraint						
Trial	G	H	I	J	K	L
Max Excur. (km)	6779	4885	3063	4680	5177	1268
Min Elev. Angle	9.20°	9.31°	9.30°	8.94°	8.60°	8.85°
No. of revs.	13	13	13	13	13	13
Ave. g (days)	4.00	3.00	2.00	3.99	3.00	2.00
Ave. h (turns)	3.37	3.42	3.61	3.24	3.14	3.26

reference. Therefore, re-initializing the control profile after the first segment is helpful to maintaining the desired trajectory. The adaptive method developed for this investigation is successful in some scenarios, based on the reference trajectory as well as the magnitude of the system errors. As mentioned, future work includes simulating the various scenarios in a Monte Carlo approach. Additional improvements include the solar sail reflectivity model (e.g., an optical or realistic sail model) and incorporating the ramp-up effects of the turns in a turn-and-hold control scheme.

Given a good initial guess for a trajectory and attitude profile in an ephemeris-based, inertial regime, the finite-difference method is adaptable to transition solutions in the Earth–Moon system to higher-fidelity representations, such as an ephemeris-based model. Effectively, the technique presented in this study, as well as the previous analyses, apply a numerical method to solve a boundary value problem based on a solution supplied by a different numerical method. This form of "bootstrapping," using the solution from one method to initialize another, is applicable to many trajectory design problems. Future work includes employing the FDM algorithm to generate an new reference path when the adaptive controller fails to converge. By constraining the current state and using the existing reference trajectory as the initial guess, the FDM can generate an updated reference path.

VI. Acknowledgments

The authors thank Laurie Mann and Diane Craig Davis of a.i. solutions, Inc., for their review of this paper. Portions of this work were supported by Purdue University and the School of Aeronautics and Astronautics. Additional support from a.i. solutions, Inc., is acknowledged.

References

[1]Tsuda, Y., Mori, O., Funase, R., Sawada, H., Yamamoto, T., Saiki, T., Endo, T., and Kawaguchi, J., "Flight Status of IKAROS Deep Space Solar Sail Demonstrator," *61st International Astronautical Congress*, Prague, Czech Republic, September 2010, Paper No. IAC-10-A3.6.8.

[2]"NASA - NanoSail-D Homepage," http://www.nasa.gov/mission_pages/smallsats/nanosaild.html, January 2012, [Website, accessed 7 July 2012].

[3]Biddy, C. and Svitek, T., "LightSail-1 Solar Sail Design and Qualification," *Proceedings of the 41st Aerospace Mechanisms Symposium*, Jet Propulsion Laboratory, Pasadena, California, June 2012.

[4]"NASA - Solar Sail Demonstration (The Sunjammer Project)," http://www.nasa.gov/mission_pages/tdm/solarsail/solarsail_overview.html, 2011, [Website, accessed 24 June 2012].

Table 5: Adaptive targeting: 3° control error (3σ) with state knowledge of 10 km in position and 10 cm/sec in velocity (3σ) and 10°/hr slew rates

Color	red-orange			dark-blue		
Initial Window, g_0 (days)	4	3	2	4	3	2
7° elevation-angle constraint						
Trial	A	B	C	D	E	F
Max Excur. (km)	14391	8049	7891	10666	1052	1282
Min Elev. Angle	10.82°	9.50°	10.77°	11.73°	17.62°	17.62°
No. of revs.	1	12	3	0	0	0
Ave. g (days)	3.56	2.96	1.91	3.60	3.00	2.00
Ave. h (turns)	3.89	3.71	4.77	3.40	3.50	3.00
5000 km excursion constraint						
Trial	G	H	I	J	K	L
Max Excur. (km)	4121	5459	4792	6208	6822	5321
Min Elev. Angle	10.07°	10.13°	9.15°	11.22°	7.35°	8.92°
No. of revs.	0	1	13	0	4	13
Ave. g (days)	4.00	2.72	2.00	3.57	2.93	1.99
Ave. h (turns)	4.00	5.22	4.17	3.71	3.84	3.54

[5]Macdonald, M. and McInnes, C., "Solar sail science mission applications and advancement," *Advances in Space Research*, Vol. 48, No. 11, 2011, pp. 1702–1716.

[6]Ozimek, M. T., Grebow, D. J., and Howell, K. C., "Design of Solar Sail Trajectories with Applications to Lunar South Pole Coverage," *Journal of Guidance, Control, and Dynamics*, Vol. 32, No. 6, November–December 2009, pp. 1884–1897.

[7]Wawrzyniak, G. G. and Howell, K. C., "Investigating the Design Space for Solar Sail Trajectories in the Earth–Moon System," *The Open Aerospace Engineering Journal*, Vol. 4, 2011, pp. 26–44.

[8]Wawrzyniak, G. G. and Howell, K. C., "Flight-path control for solar sail spacecraft," *22nd AAS/AIAA Space Flight Mechanics Meeting, Charleston, South Carolina*, January 2012.

[9]Wawrzyniak, G. G. and Howell, K. C., "Generating Solar Sail Trajectories in the Earth–Moon System Using Augmented Finite-Difference Methods," *International Journal of Aerospace Engineering*, Vol. 2011, 2011, Article ID 4776197, 13 pages.

[10]Standish, E. M., "JPL Planetary and Lunar Ephemerides, DE405/LE405," Interoffice Memorandum IOM 312.F - 98 - 048, Jet Propulsion Laboratory, Pasadena, California, 1998.

[11]Folkner, W. M., Standish, E. M., Williams, J. G., and Boggs, D. H., "Planetary and Lunar Ephemerides DE 418," Interoffice Memorandum IOM 343R-07-005, Jet Propulsion Laboratory, Pasadena, California, 2007.

[12]Folkner, W. M., Williams, J. G., and Boggs, D. H., "The Planetary and Lunar Ephemerides DE 421," Interoffice Memorandum IPN Progress Report 42-178, Jet Propulsion Laboratory, Pasadena, California, August 2009.

[13]Navigation and Ancillary Information Facility, "NAIF Mice Toolkit Hypertext Documentation," http://naif.jpl.nasa.gov/pub/naif/toolkit_docs/MATLAB/, June 2011, [Website, accessed 7 July 2012].

[14]Campbell, B., *An Analysis of Thrust of a Realistic Solar Sail with Focus on a Flight Validation Mission in a Geocentric Orbit*, Ph.D. Dissertation, The George Washington University, Washington, DC, May 2010.

[15]Greenwood, D. T., *Principles of Dynamics*, Prentice Hall, Upper Saddle River, New Jersey, 2nd ed., 1988.

[16]Danby, J. M. A., *Fundamentals of Celestial Mechanics*, Willmann-Bell, Inc., Richmond, Virginia, 2nd ed., 1988.

[17]Vallado, D., *Fundamentals of Astrodynamics and Applications*, Microcosm Press, Hawthorne, California, 2007.

[18]Russell, R. P., "Survey of Spacecraft Trajectory Design in Strongly Perturbed Environments," *Journal of Guidance, Control, and Dynamics*, Vol. 35, No. 3, May–June 2012, pp. 705–720.

[19]McInnes, C. R., *Solar Sailing: Technology, Dynamics and Mission Applications*, Space Science and Technology, Springer-Praxis, New York, 1999.

[20]Rios-Reyes, L. and Scheeres, D. J., "Solar-Sail Navigation: Estimation of Force, Moments, and Optical Parameters," *Journal of Guidance, Control, and Dynamics*, Vol. 30, No. 3, May–June 2007, pp. 660–668.

[21]Ozimek, M. T., Grebow, D. J., and Howell, K. C., "A Collocation Approach for Computing Solar Sail Lunar Pole-Sitter Orbits," *The Open Aerospace Engineering Journal*, Vol. 3, 2010, pp. 65–75.

[22]Wawrzyniak, G. G. and Howell, K. C., "Numerical techniques for generating and refining solar sail trajectories," *Advances in Space Research*, Vol. 48, No. 11, 2011, pp. 1848–1857.

[23]Wawrzyniak, G. G. and Howell, K. C., "Trajectory Control for a Solar Sail Spacecraft in an Offset Lunar Orbit," *61st International Astronautical Congress*, Prague, Czech Republic, September 2010, Paper No. IAC-10.C1.2.3.

[24]Akima, H., "A New Method of Interpolation and Smooth Curve Fitting Based on Local Procedures," *Journal of the Association for Computing Machinery*, Vol. 17, No. 4, October 1970, pp. 589–602.